CALIFORNIA INSTITUTE OF TECHNOLOGY

Lindhurst Laboratory of Experimental Geophysics
Seismological Laboratory 252-21, 1200 E. California Blvd.
Pasadena, CA 91125

Thomas J. Ahrens
Professor of Geophysics

June 7, 2002

"Impact Cratering Calculations"

NASA NAG5-10208

Final Report

October 1, 2000 to September 30, 2001

Thomas J. Ahrens
Principal Investigator

cy:
Dr. David Senske (NASA)
Adrian Jefferson, NASA Grants Officer
ONR, San Diego
NASA Center for Aerospace Information, Hanover MD
Spons. Res.
Patents Office
Project Accounting (letter only)

E-MAIL: tja@caltech.edu • TELEPHONE# (626) 395-6906 • FAX# (626) 564-0715, 568-0935
WEB ADDRESS: http://www.gps.caltech.edu/~ahrens

I. Work Accomplished

A. Impact on Mars

One major result of studying impact cratering on Mars is given in:

1. Stewart, S. T., J. D. O'Keefe, and T. J. Ahrens, Formation of fluidized ejecta blankets on Mars by shock-melting subsurface ice, Science, submitted, 2002.

Many Martian craters are surrounded by ejecta blankets which appear to have been fluidized [*Barlow*, 1988; *Mouginis-Mark*, 1978] forming lobate and layered deposits terminated by one or more continuous distal scarps, or ramparts. One of the first hypotheses for the formation of so-called rampart ejecta features was shock-melting of subsurface ice, entrainment of liquid water into the ejecta blanket, and subsequent fluidized flow [*Carr et al.*, 1977; *Mouginis-Mark*, 1979]. Our work quantifies this concept. Rampart ejecta found on all but the youngest volcanic and polar regions, and the different rampart ejecta morphologies [*Barlow et al.*, 2000] are correlated with crater size and terrain [*Barlow and Bradley*, 1990; *Mouginis-Mark*, 1979]. In addition, the minimum diameter of craters with rampart features decreases with increasing latitude [*Kuz'min et al.*, 1988] indicating that ice laden crust resides closer to the surface as one goes poleward on Mars (Fig. 1).

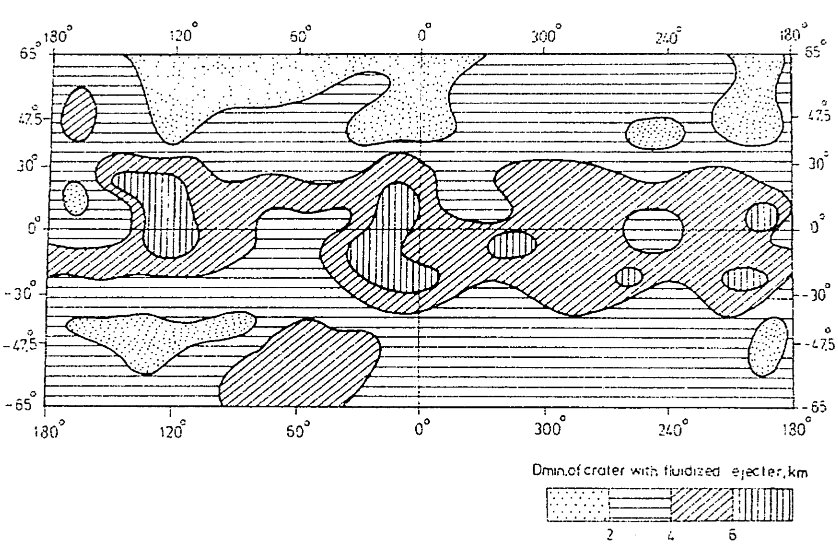

Fig. 1. Geographic distribution of the onset of rampart (fluidized ejecta) craters on Mars. Onset diameters are greatest near the equator, indicating the depth (~ 1 km) to interstitial ice in the crust is greatest in the tropics (after Squyres et al. [1992])

Our ability to interpret the cratering record to learn about water on Mars has been limited by our understanding of the physical processes which fluidize ejecta blankets and the competing hypothesis that rampart morphologies may be produced by interactions between the ejecta curtain and the atmosphere [*Barnouin-Jha and Schultz*, 1998; *Schultz*, 1992; *Schultz and Gault*, 1979].

In Paper 1, we report on the results from numerical simulations of impact cratering onto an ice-rich Martian regolith, including the projectile and ejecta flow through the atmosphere, and the implications for formation of fluidized ejecta and global crustal water content.

Recently, we have experimentally demonstrated from our measured shock properties of H_2O ice [*Stewart and Ahrens*, 2002] that shock-induced melting begins at shock pressures of only 0.6 GPa under terrestrial conditions, more than an order of magnitude lower than the 6.2 to 10 GPa previously inferred [*Ahrens and O'Keefe*, 1985; *Kieffer and Simonds*, 1980]. Ice in the Martian crust, at temperatures between 150 and 273 K, will begin to melt after experiencing shock pressures between 2.2 and 0.6 GPa, respectively, and will completely melt upon release from shock compression to pressures above 6 and 3.7 GPa.

We conducted long duration simulations of crater formation by asteroid-derived impactors onto an ice-filled Martian regolith, starting with the projectile several atmospheric scale heights above the surface (30 to 60 km) and continuing through the formation of the ejecta blanket and collapse of the impact vapor plume. Using the finite-difference, Eulerian-Lagrangian hydrocode CTH [*McGlaun et al.*, 1990], normal impacts were simulated using two-dimensional cylindrical symmetry. The spatial resolution of the Eulerian mesh was constrained to 20-30 cells across the projectile radius, and the width and depth of the simulated crust were about an order of magnitude larger than the final crater size to minimize edge effects. Several hundred massless Lagrangian tracer particles were distributed through the crust to track the shock pressure decay profile with depth, ejection angles and velocities, and the excavated zone.

The model crust and atmosphere were initialized as isothermal layers in gravitational equilibrium with a surface pressure of 7 mbar. The initial temperatures of the atmosphere and crust were 170 and 200 K, respectively, which is representative of Martian mid-altitudes and mid-latitudes. We considered a range of ground ice content using an exponential decay profile to simulate a theoretical regolith with ice-filled cracks and pore spaces each computation cell representing the crust was initialized with the specified ice and rock volume fractions under lithostatic pressure, and the explicit equation of state for each material is utilized throughout the computation. By assuming equal shock pressures in the ice and silicate fraction, upon partial melting ice marked strength reduction follows as we volume averaged yield strength in the mixture. The atmosphere is considered a pure CO_2 ideal gas. Asteroidal impactors and the Martian crust are probably basaltic in composition. However, a shock equation of state for dunite ANEOS [*Thompson and Lauson*, 1972] was used as an approximation. In mixed cells, equations of state for each component, the CO_2 atmosphere, silicate projectile and crust, and H_2O ice, are used to calculate shock pressures and temperatures. The unmelted dynamic strength of the Martian crust is constrained by the observed transition diameter, D_T, from simple to complex craters on Mars, ~7 km [*Garvin et al.*, 2002]. Our previous cratering studies (Eq. 28, O'Keefe and Ahrens [1993]) define an effective yield strength of 10^7 Pa [*O'Keefe and Ahrens*, 1999; *O'Keefe et al.*, 2001] for Mars. We varied the projectile diameter (100-2000 m) to simulate simple, transition and complex type crater formation at typical asteroidal impact velocities, 10 km/s.

The shock wave pressure decays exponentially with distance from the impact point [*Melosh*, 1989]. Using the pressure decay profile, we calculate the radial extent of impact-induced melting of ground ice. The flow field of the Lagrangian tracer particles determines the zone of excavation used to calculate the fraction of ice melted within the ejecta blanket.

The results of the simulations are summarized in Fig. 2. The transient crater diameter corresponds to the hemispheric diameter at the maximum depth of penetration, and the final crater diameter is given by the location of the overturned ejecta flap. The crater diameters are in very good agreement with the crater scaling laws developed for competant rock surfaces. The depths for shock-induced partial and complete melting were determined from the shock-pressure decay profiles, Fig. 3. For rocky impactors at 10 km/s, the peak shock pressures are just above 100 GPa, and very little rock or ice is vaporized. The bulk of material excavated into the continuous ejecta blanket originates from the zones of complete and partial melting, Fig. 4. For a near-surface ground ice content of 20% (by volume), we find that the hemispherical volume where subsurface ice is partially melted by the impact shock has a radius of about 14 projectile radii (r_p), and ice is completely melted within about 7 r_p. Partial melting of ground ice occurs throughout the excavation zone. The extent of melting will slightly increase as the composition approaches pure rock (Fig. 3), although the melt zone is expected to be slightly smaller for the more common oblique impact events [*Pierazzo and Melosh*, 2000]. Also, shock-induced melting may be more efficient if the ice has significant salt content. The presence of 0-20% (by volume) ground ice increases the diameter of the final crater by only a fraction of a projectile radius (Fig. 4A and B).

The material ejected near the crater rim originates from both the completely and partially melted zones (Fig. 4), and more than half the ice which is excavated into the continuous ejecta blanket is melted. For 10 km/s impacts, the ejection velocities decrease from almost 3 km/s near the impact point to 10's m/s near the crater rim. Thus, the solid ejecta curtain following approximately ballistic trajectories will impact the surrounding terrain with horizontal flow velocities in the range of 10's-100's of m/s, within the range of large terrestrial landslides.

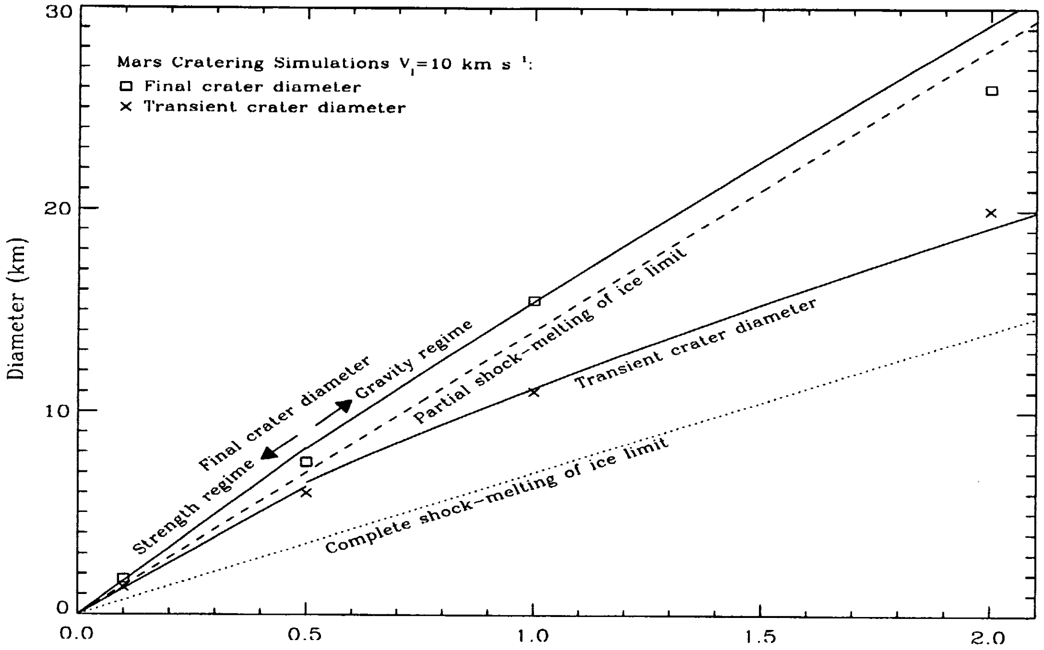

Fig. 2. Transient (×) and final (□) crater diameter as a function of projectile diameter for typical asteroid-derived impactors on Mars. Diameter of hemispherical zone of partial melting of ground ice (dashed line) is comparable to final crater diameter. Size of zone of complete melting (dotted line) is about half the transient crater cavity. Solid lines correspond to crater scaling functions in competent rock [*Melosh*, 1989].

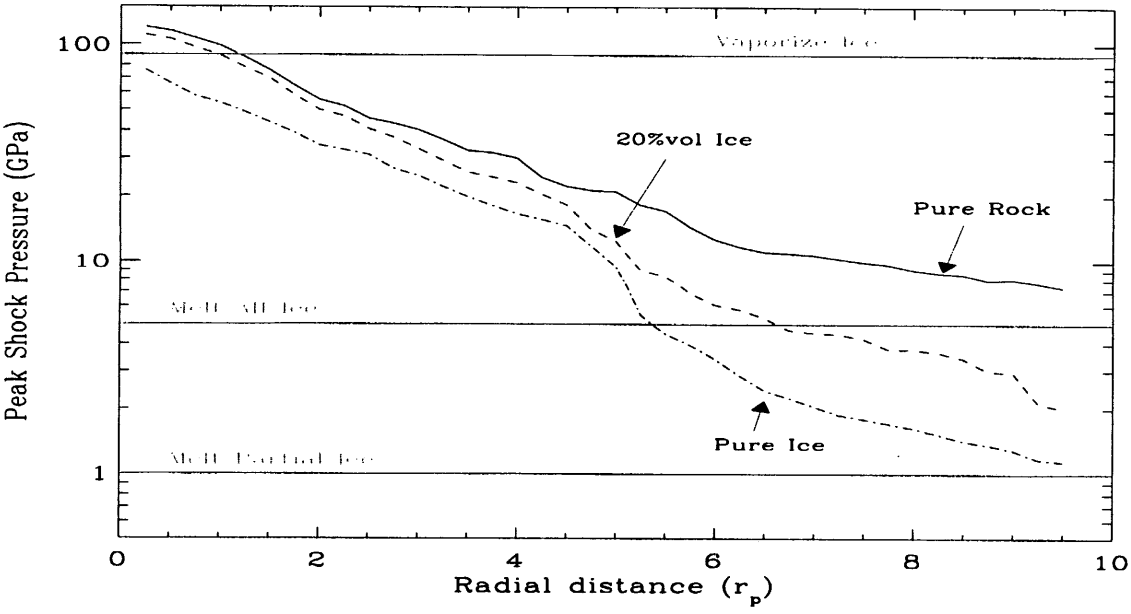

Fig. 3. Shock pressure decay profiles for different Martian crust composition. Horizontal lines indicate critical shock pressures for partial and complete melting and complete vaporization.

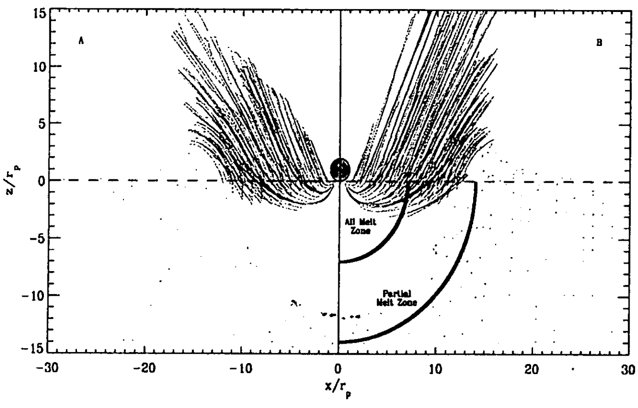

Fig. 4. Crater excavation zones for 500 m diameter projectile impacting at 10 km/s into (A) pure rock and (B) a 20% (volume) ice-rock mixture. Trajectory histories shown for Lagrangian tracer particles (×) from within the excavated crater cavity. Ejecta trajectories shown for computation with no atmosphere at 20 sec.

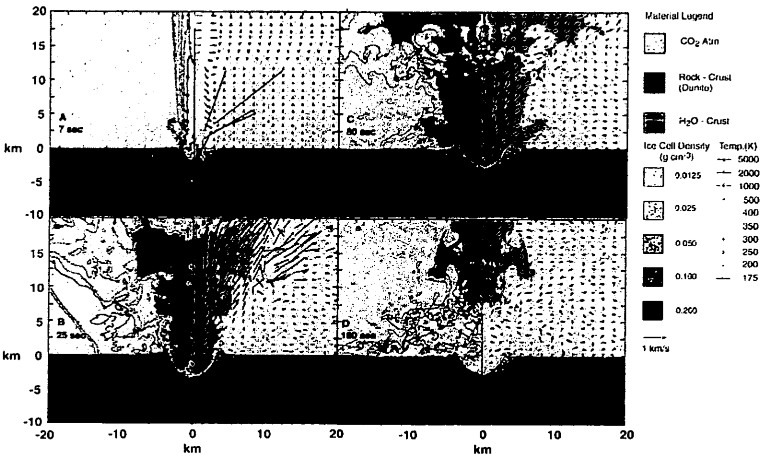

Fig. 5. Time sequence for 500 m diameter projectile impact onto regolith with 20% (volume) near-surface ice, including Martian atmosphere. Each panel shows ice content (left, shading), temperature contours (left), flow field velocities (right), and major material composition (solid colors).

Fig. 5 displays a time series from a simulation with 500 m-diameter projectile, forming a 7.5-km diameter crater, showing the atmospheric shock (A), ejecta curtain, and interaction with the vapor plume, and collapse of the impact vapor plume. For simple craters, with $D \leq 7$ km, the water vapor plume is contained by the mass of the atmosphere and does not spread far beyond the crater rim. For large craters, D>10's km, a portion of the water vapor mass may be dispersed into the upper atmosphere, transiently affecting the regional and perhaps global climate, and remaining mass of the plume collapses down over the crater and ejecta blanket as transient rain or sleet. For transition size craters, D~7 km, the vapor plume appears to interact with the solid ejecta curtain during the formation of the continuous ejecta blanket. Figs. 6-8 summarize the simulations for a 0.1, 0.5, and 2 km diameter silicate impactors.

Models for the formation of rampart morphologies by fluidized flow [*Ivanov*, 1996] suggest a conservative liquid water volume fraction, corresponding to a near-surface ice volume fraction of about 20-40%. Using the observed rampart ejecta craters [*Barlow and Bradley*, 1990], corrected for observational bias using the Martian crater production function [*Hartmann*, 1999]. Summing over the entire Martian rampart crater size range, D=1-32 km, the volume of ice implied by the observed Martian rampart crater number distribution is 20% which is equivalent to a global layer of water about 0.6 m deep. Based on the crater production function, this value corresponds to the amount of ice excavated by impact craters over the past 3 Ga. Since rampart craters stochastically sample a fraction of the surface, limited to excavation depths within the upper 2 km for the observed size range, the actual regolith ice content must be considerably larger. Only 0.5 % of the Martian surface area was sampled by the observed rampart craters. Correcting for the sampling area, the implied total ice content, within 2 km of the surface, is equivalent to a global layer of water about 120 m thick.

B. Impact Damage and Porosity Cratering Studies

Our major results in this area are in:

2. O'Keefe, J. D., S. T. Stewart, M. E. Lainhart, and T. J. Ahrens, Damage and rock-volatile mixture effects in impact crater formation, Int. J. Impact Engng, 26, 543-553, 2001.
3. O'Keefe, J. D. and T. J. Ahrens, Hydrodynamic instabilities and impact cratering, submitted to Nature [2002].

Our goal in Paper 2 was to determine what strength model(s) reproduce the faults and complex features found in large scale gravity driven craters. Collapse features found in large scale craters require that the rock strength weaken as a result of the shock processing of rock and the later cratering shear flows (e.g. Melosh and Ivanov [1999]). In addition to the presence of molten silicate in the intensely shocked region, the presence of water, either ambient, or the result of shock melting of ice weakens rock. There are several other mechanisms for the reduction of strength in geologic materials including dynamic tensile and shear induced fracturing (e.g. Melosh and Ivanov [1999]). Fracturing is a mechanism for large reductions in strength. We found that by incorporating damage into the models that we could in a single integrated impact calculation, starting in the atmosphere produce final crater profiles having the major features found in the field measurements [*Morgan et al.*, 1997] (central uplifts, inner ring, terracing and faulting. This was accomplished with undamaged surface strengths (~0.1GPa) and in depth strengths (~1.0 GPa).

We modeled the damage in geologic materials using a phenomenological approach, which coupled the Johnson-Cook damage model [*Johnson and Holmquist*, 1994]. with the CTH code geologic strength model. The objective here was not to determine the distribution of fragment sizes, but rather to determine the effect of brecciated and comminuted material on the crater evolution, fault production, ejecta and final crater morphology. There are a number of definitions of damage which are discussed by Kachanov [1986]. Damage (D) here is defined as the ratio of the integrated plastic strain experienced by a given material particle relative to the integrated plastic strain required at failure (loss of strength). The time derivative of damage is given by

$$dD/dt = (d\varepsilon/dt) /\varepsilon_f \qquad (1)$$

where $d\varepsilon /dt$ is the plastic strain rate. The integrated plastic strain at failure, ε_f is defined by

$$\varepsilon_f = (\varepsilon_{f0} + \varepsilon_{fduc} \exp(- \varepsilon_{fP} P/ Y_0)*(1 + \varepsilon_{f\,d\varepsilon/dt} \ln (d\varepsilon/dt))*(1 + \varepsilon_{fT} (T-T_r)/(T_m-T_r)) \qquad (2)$$

and ε_{f0} , ε_{fduc} , ε_{fP} , $\varepsilon_{f\,d\varepsilon/dt}$, and ε_{fT} , are material parameters, P and T are the local pressure and temperature and T_m and T_r are the melt temperature and the thermal softening temperature, Y_0 is the undamaged Mohr-Coulomb yield strength at zero pressure, ε_{f0} is a measure of the magnitude of the strain at failure at ambient temperature and zero pressures. ε_{fP} is a measure of the rate of increase of ductility with pressure and hence the transition from brittle to ductile behavior [*Scholz*, 1990]]. $\varepsilon_{f\,d\varepsilon/dt}$ is a measure of the rate of change in ε_f due to strain rate effects, and is important for small scale impacts, and is not as important for large scale late stage shear flows. ε_{fT} is a measure of the increase in ductility due to thermal effects. The above parameters have been determined for a number of metals , concrete and some ceramics. Rocks have had little work. Recently, more laboratory damage data has become available on geologic materials on account of efforts of researchers at LLNL [*Lomov et al.*, 2001] and LANL [*Swift et al.*, 2000]..

The damaged strength at zero pressure is a function of thermal softening, and damage and is given by

$$Y_{0d} = Y_{dT} (1-D) \qquad (3)$$

where Y_{dT} is the thermally and density degraded strength at zero pressure. The damage function is unity at failure and zero when there is no degradation. This reduction in strength was incorporated into the geologic strength model to account for pressure effects (Mohr-Coulomb) and is given by

$$Y_s = Y_{vm} + (Y_{0d} -Y_{vm}) \exp\{ -dY_s/dP^* P /(Y_{vm}-Y_{0d}) \} \qquad (4)$$

where Y_{vm} is the limiting strength at high pressure (von Mises magnitude). The internal angle of friction

aa105

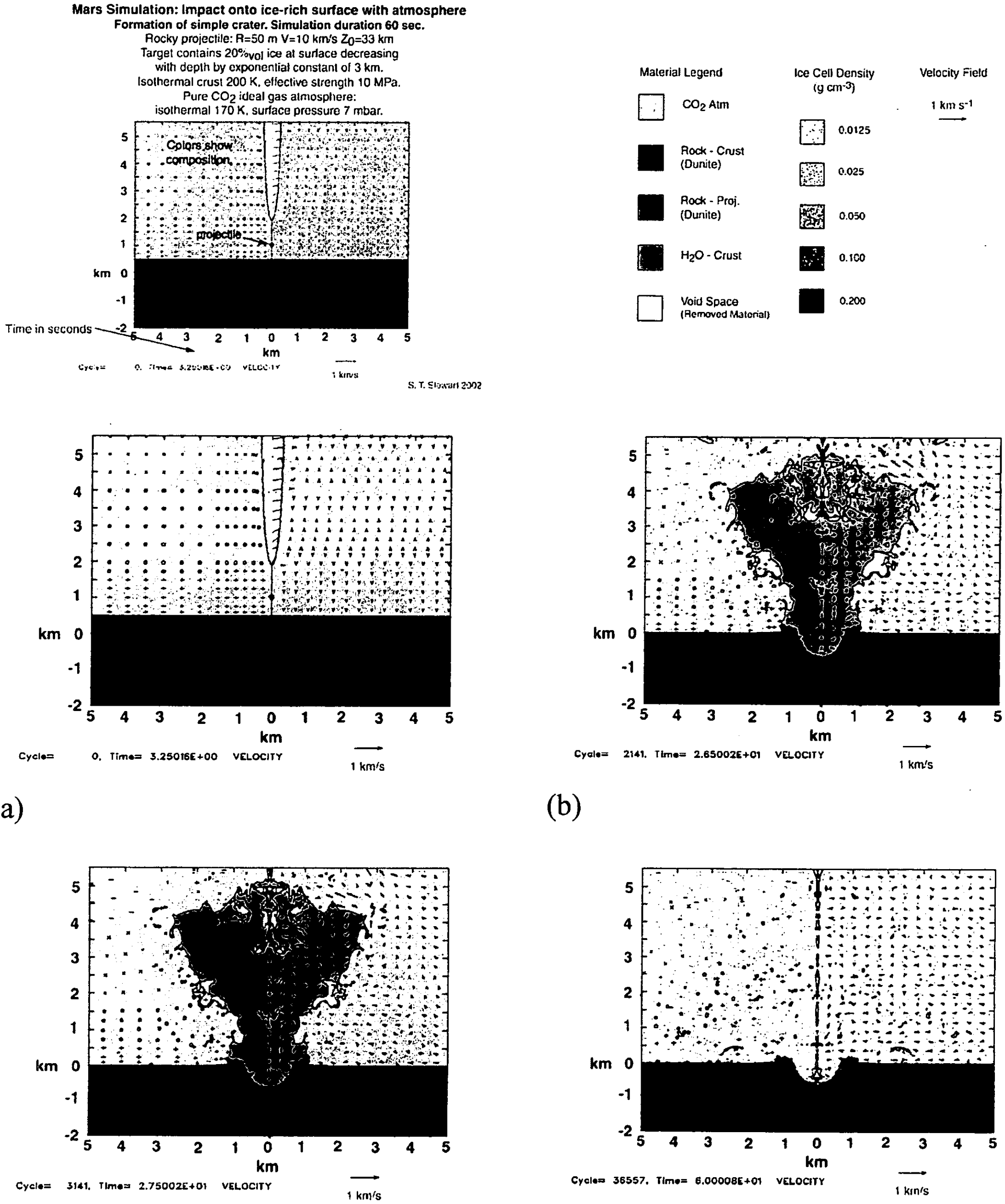

(a) (b)

(c) (d)

Fig. 6. Particle velocity, material field and ice contents for 50 m radius silicate impactor intersecting with CO_2 atmosphere, 20% icy surface of Mars @ 10 km/sec. (a) Time = 3.25 sec projectile 1-km above surface. (b) Time = 26.5 sec. water vapor plume has expanded over transient cavity; 1.8 km in diameter. (c) Time = 27.5 sec water vapor plume starting to collapse. (d) Time = 60.0 sec vapor plume has collapsed and Mars' atmosphere is reestablished above 1.8 km diameter crater that has not been modified.

aa103

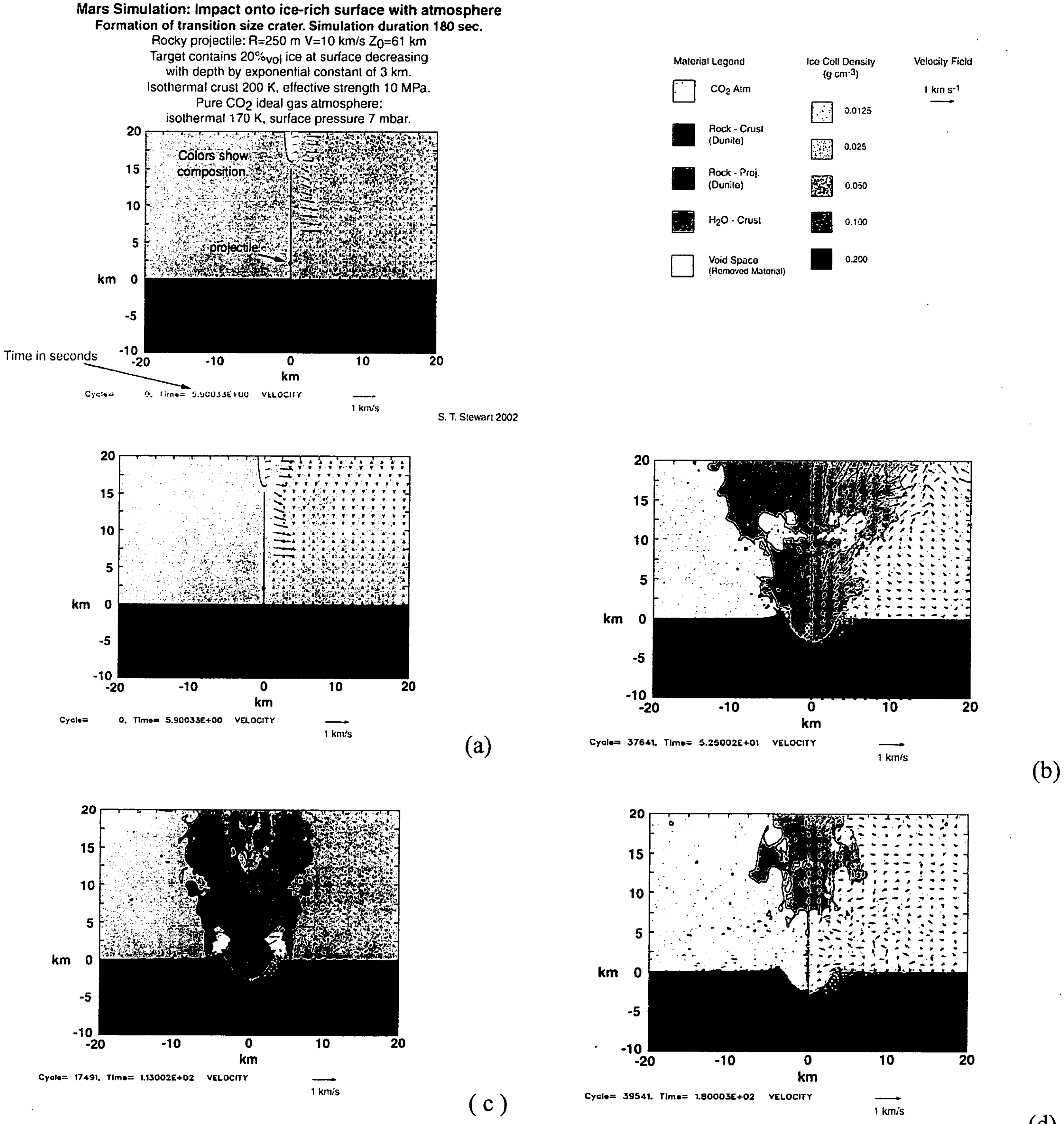

Mars Simulation: Impact onto ice-rich surface with atmosphere
Formation of transition size crater. Simulation duration 180 sec.
Rocky projectile: R=250 m V=10 km/s Z_0=61 km
Target contains 20%$_{vol}$ ice at surface decreasing
with depth by exponential constant of 3 km.
Isothermal crust 200 K, effective strength 10 MPa.
Pure CO_2 ideal gas atmosphere:
isothermal 170 K, surface pressure 7 mbar.

S. T. Stewart 2002

Fig. 7. Particle velocity and material field and ice contents for 250 m radius impactor impacting Mars. (a) Time = 5.9 sec, projectiles is 2 km above surface. (b) Time = 52.5 sec. Transient crater, 6 km iin diameter formed and vapor plume has risen to ~50 km altitude. (c) Time = 113 sec. Transient cavity is slightly relaxing as water plume collapses. (d) Time = 180 sec. Crater slightly collapses as CO_2 atmosphere is established above crater.

aa102

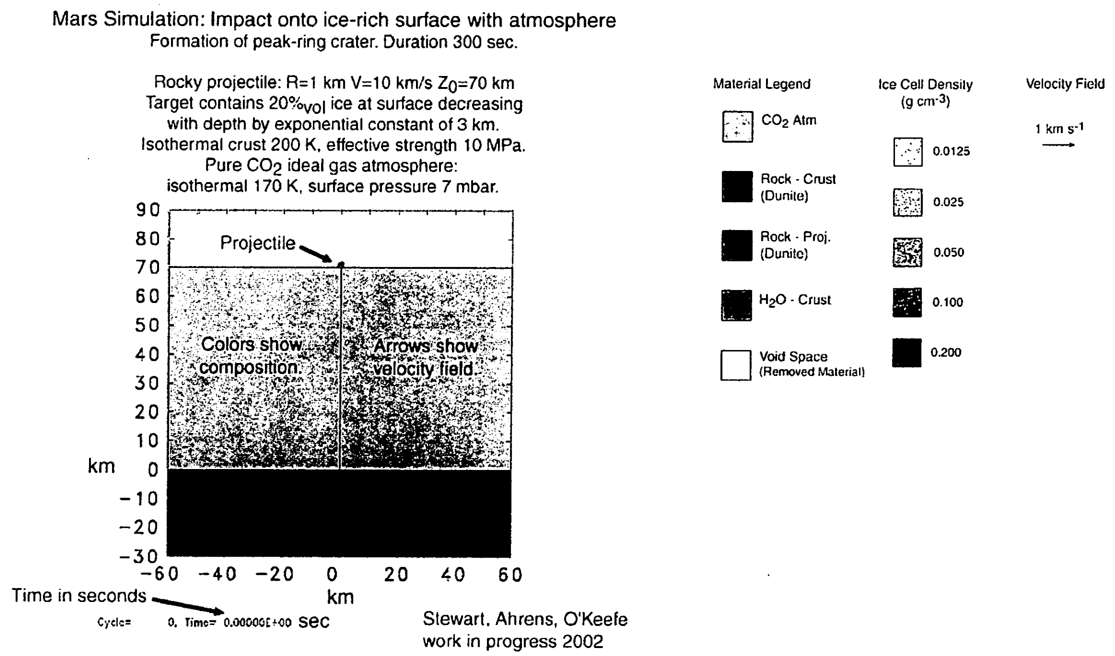

Mars Simulation: Impact onto ice-rich surface with atmosphere
Formation of peak-ring crater. Duration 300 sec.

Rocky projectile: R=1 km V=10 km/s Z_0=70 km
Target contains 20$\%_{vol}$ ice at surface decreasing
with depth by exponential constant of 3 km.
Isothermal crust 200 K, effective strength 10 MPa.
Pure CO_2 ideal gas atmosphere:
isothermal 170 K, surface pressure 7 mbar.

Stewart, Ahrens, O'Keefe
work in progress 2002

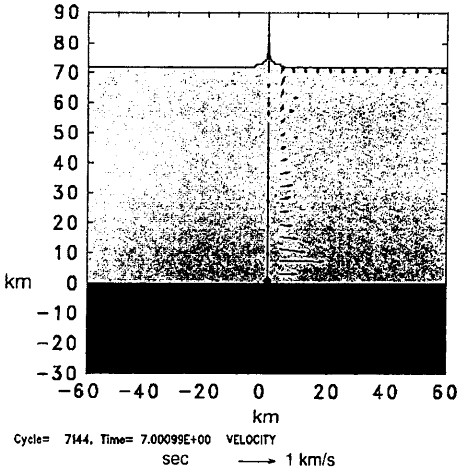

(a)

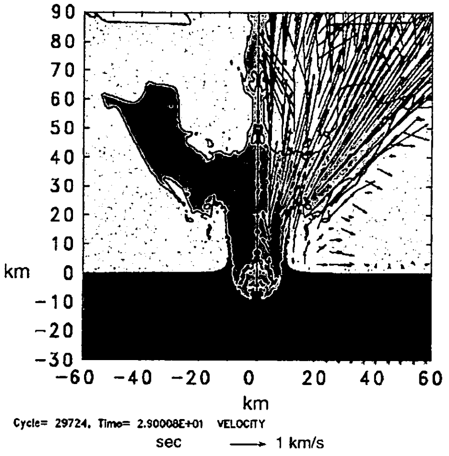

(b)

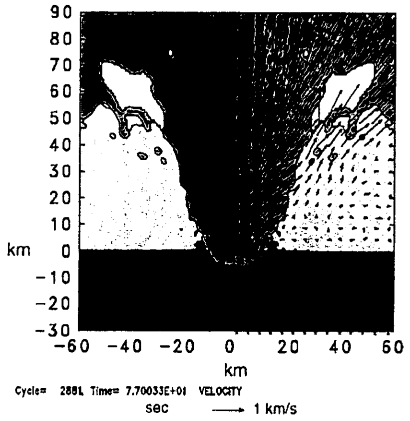

(c)

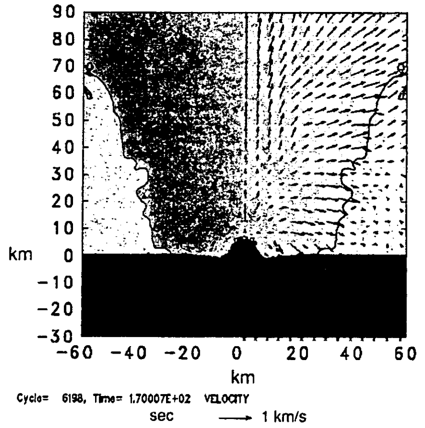

(d)

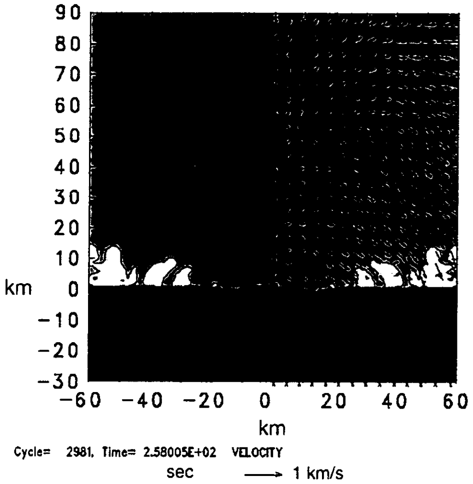

(e)

Fig. 8. Particle velocity and material field and ice contents for 1 km radius impactor, impacting Mars. (a) Time – 7 sec. Projectile is just striking planet. (b) Time – 29 sec. Transient cavity formed, 18 km in diameter and 100 km vapor plume driven into atmosphere. (c) Time – 77 sec. Transient cavity is collapsing. (d) Time – 70 sec. Central peak extends 5 km upwards. (e) Time – 258 sec. Central peak has collapsed leaving ringed crater structure ~ 40 km in diameter. Local atmosphere remains as vaporized water gas from regolith.

also degrades with damage and is given by

$$dY/dP = dY/dP]_{Dam} - (1-D)\{ dY/dP]_{unDam} - dY/dP]_{Dam} \} \qquad (5)$$

where $dY/dP]_{unDam}$ and $dY/dP]_{Dam}$ are the undamaged and damaged measures of internal friction. The above yield surface is plotted in Fig 9. In the case of no damage, and at high pressures, the yield strength is the von Mises limit. At zero pressure , the yield strength is given by Y_{0d} (eqn 4), and under extensive conditions, failure (zero yield strength) occurs at the tensile failure limit, $-T_f$. In the case of complete damage, the yield strength is zero at zero pressure and increases with confining /overburden pressure. at a rate depending upon dY/dP (eqn. 5). The yield surface limit at high pressures is given by the damaged von Mises limit, Y_{vmd} . The shape of the damaged yield surface depends upon the degree of damage to the internal angle of friction, dY/dP (eqn. 5). Examples of damage zone for an impact representative of the Chicxulub event and the effect of overburden pressure on the local strength during that impact is shown in Fig10.

We accomplished our goal of determining whether or not the damage approach to was capable of reproducing faults and complex features found in large scale craters with plausible assumptions for the magnitudes of the material parameters. In general, we only found faulting when damage was modeled. Specifically, we performed parametric variations on the magnitudes of some of the key material constants to determine if that resulted in plausible values for ε_f and dY/dP and to determine if these would result features such as in inner rings, central peaks and faults. In the expression for ε_f , we varied ε_{f0} and set the other parameters to zero. This bounds the magnitude of ε_f . since the other terms in general increase the magnitude of ε_f .We found that for the Chicxulub impact case, that the parameter ranges for central uplift and inner ring formation are when the in depth strength (Y_{vm}) < 1.0GPa, the internal friction angle <45 deg. and the ε_f is <0.15. We found for the conditions for fault scarps and slumping/terracing to form are when the impactor diameter is greater than 15 km , the damaged value of the internal angle of friction < 30 deg. and $\varepsilon_f \sim < 0.08$. These integrated strain to failure values for both collapse and fault features are within the broad range of laboratory measurements. Strain at fault measurements of rock specimens under confining pressure can vary from 0.03 to 0.25 (0.2GPa confining pressure). Rocks within a large scale impact environment can be expected to have values >0.1, because of shock heating and environmental thermal and pressure distributions [*Brace et al.*, 1966].

Dilatancy has long been recognized as an important aspect of rock response [*Brace et al.*, 1966]; it is produced by the creation of cracks from inhomogeneous stresses during loading and at low pressures it results in a porous, decreased density, rock. (Fig.11). We have developed a first order model for bulking. The model is a relationship between the degree of damage, pressure, and density. This is shown in Figure 11. For undamaged rock, the density increases inversely with the magnitude of the bulk modulus. For completely damaged rock, which can be characterized as gravel, the density is 20 to 40% less than undamaged or competent rock. We assume that the gravel density is the limiting density of damaged rock at zero pressure. The bulk moduli has been measured for many gravels and its magnitude is much less than the competent rock The density of the damaged rock(gravel) also increases with the inverse of the gravel bulk modulus. With increasing pressure, the cracks close and the material locks together at a pressure determined to be the intersection of the bounding density curves. This point is shown in Fig 11. We also assume that the damaged density at zero pressure varies at linearly with damage and the magnitude of the calculated bulk modulus requires the density- pressure curve to intersect at the bounding intersection point. (see Fig 11). An example of the effect of bulking on crater profile is shown in Fig. 12. The decrease in the crater depth correlates directly with the decrease in rock density due to fracture shown in Fig. 11.

In our recent survey (Paper 3) of hydrodynamic instabilities in various planetary hypervelocity impact scenarios, we have explored a very wide range of impacts of both similar and strongly dissimilar projectile/target density ratios, $DR = \delta/\rho$ where δ is projectile density and ρ target density and VN is the vaporization number U^2/E_v. What we found is that when the specific kinetic projectile energy far exceeds the target vaporization energy target instabilities always form (Fig. 13). The regime previously explored by Holsapple and Schmidt [1982] in which the projectile spreads and smoothly lines the transient crater cavity occurs only in the case of $VN \leq 10$ and $DR \leq 3$. For greater values of VN and DR, projectile or target/RT (Rayleigh-Taylor) or K/H (Kelvin-Helmholtz) instabilities grow faster than the slowing of the projectile by the target material. Thus these instabilities control transient crater growth

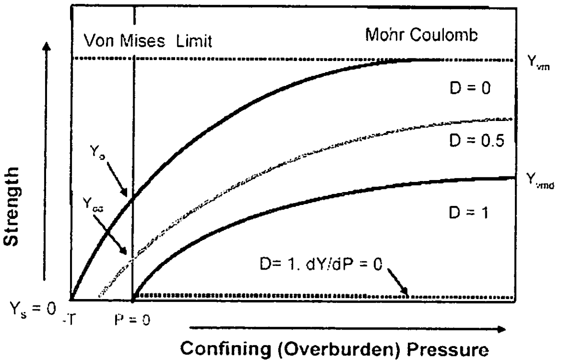

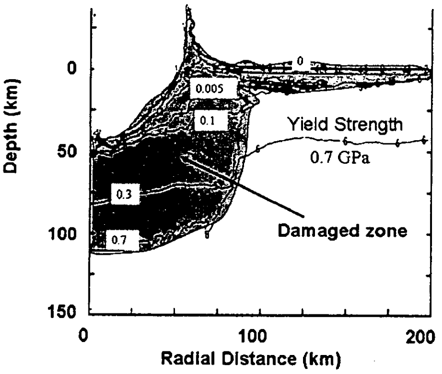

Fig. 9.

Fig. 10

Fig. 9. Diagram of the yield surface as a function of normalized pressure. Top curve is case of no damage (D=0.0) and bottom case is complete dqamage (D=1.0).

Fig. 10. An example of the effect of damage on the yield strength distribution. Note the strength in the damaged cavity due to the overburden pressure. The magnitude of this yield strength depends upon dY/dP. If this is zero, then there is no strength in the damaged cavity and the material acts like a liquid, and would not exhibit features such as inner rings and central peaks. The time is 40 s and is at the time of maximum penetration. Impact is representative of Chicxulub event, velocity = 20 km/s, diameter = 12 km.

and the final crater profile. Moreover, or VN < 10 and DR > 3, the ejecta mass and velocity decrease with DR, with no ejecta for DR $\gtrsim 10$.

An example of the changes in the key final crater measures with increasing DR is shown in Fig. 14. The changes in the density ratio was accomplished by varying the density of the projectile or by varying the porosity of the target, which in both cases was gravity with a strength of 0.1 GPa. The present calculations, predict that for a solid granite projectile impacting a solid granite target a normalized volume, V/a^3, of 638. Holsapple's formula predict a volume of 264. Moreover, the present calculations predict a much faster increase in normalized volume with increasing values of DR (Fig. 14) than is predicting by similarity scaling theory and also discontinuous changes in final crater measures (Fig. 14).

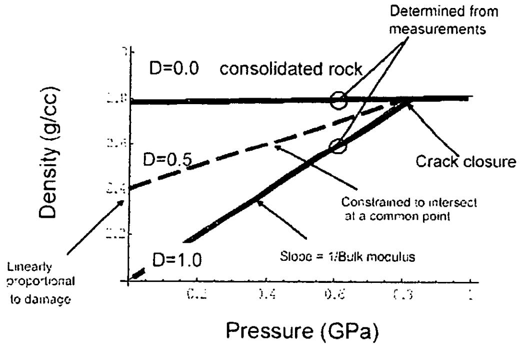

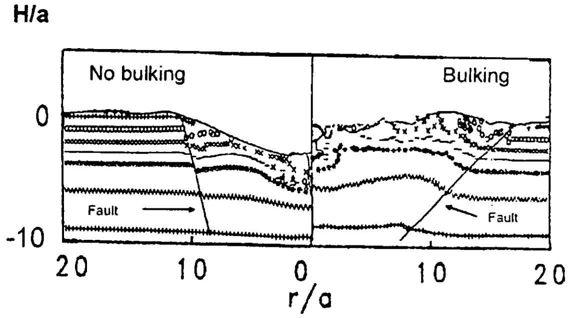

Fig. 11. Loading paths for dilatancy. Model is constrained by properties of consolidated rock at zero damage and granular material at complete (D=1.0) damage. Material would initially load along its D = 0.0 line until completely damaged, and if completely damaged, unload along the release adiabat (D=1.0) line.

Fig. 12 Final crater profiles for cases showing the effect of dilatancy [*O'Keefe and Ahrens*, 2000]. Note decreased crater depth with bulking. The impact dimensionless parameters are $Y_m/\rho U^2 = 2\times10^{-4}$ and $ga/U^2 = 3.4 \times 10^{-5}$, where U = impact velocity, ρ = target density, a = radius.

References:

Ahrens, T.J., and J.D. O'Keefe, Shock vaporization and the accretion of the icy satellites of Jupiter and Saturn, in *Ices in the Solar System*, edited by J. Klinger, D. Benest, A. Dollfus, and R. Smoluchowski, pp. 631-654, NATO ASI Series (D. Reidel), Nice, France, 1985.

Barlow, N.G., Crater size-frequency distributions and a revised Martian relative chronology, *Icarus*, *75*, 285-305, 1988.

Barlow, N.G., J.M. Boyce, F.M. Costard, R.A. Craddock, J.B. Garvin, S.E.H. Sakimoto, R.O. Kuzmin, D.J. Roddy, and L.A. Soderblom., Standardizing the nomenclature of Martian impact crater ejecta morphologies, *J. Geophys. Res.*, *105*, 26733-26738, 2000.

Barlow, N.G., and T.L. Bradley, Martian impact craters: Correlations of the ejecta and interior morphologies with diameter, altitude, and terrain, *Icarus*, *87*, 156-179, 1990.

Barnouin-Jha, O., and P. Schultz, Lobateness of impact ejecta deposits from atmospheric interaction, *J. Geophys. Res.*, *103*, 25739-25756, 1998.

Brace, W.F., B.W. Paulding, Jr., and C. Scholz, Dilatancy in the fracture of crystalline rocks, *J. Geophys. Res.*, *71*, 3939-3953, 1966.

Carr, M.H., L.S. Crumpler, J.A. Cutts, R. Greeley, J.E. Guest, and H. Masursky, Martian impact craters and emplacement of the ejecta by surface flow, *J. Geophys. Res.*, *82*, 4055-4065, 1977.

Garvin, J.B., S.E.H. Sakimoto, J.J. Frawley, and C. Schnetzler, Global geometric properties of Martian impact craters, Proc. Lunar Planet. Sci. Conf., 33, abstract, 1255, 2002.

Hartmann, W.K., Martian cratering VI: Crater count isochrons and evidence for recent volcanism from Mars Global Surveyor, *Meteoritics Planet. Sci.*, *34* (2), 167-177, 1999.

Holsapple, K.A., and R.M. Schmidt, On the scaling of crater dimensions, 2: Impact processes, *J. Geophys. Res.*, *87*, 1849-1870, 1982.

Ivanov, B.A., Spread of ejecta from impact craters and the possibility of estimating the volatile content of the martian crust, *Solar System Research*, *30*, 43-58, 1996.

Johnson, G.R., and T.J. Holmquist, An improved computational model for brittle materials, in *High-Pressure Science and Technology-1993*, edited by S.C. Schmidt, J.W. Shaner, G.A. Samara, and M. Ross, pp. 981-984, AIP Press, Woodbury, NY, 1994.

Kachanov, L.M., *Introduction to Continuum Damage Mechanics*, Martinus Nijhoff, Dordrecht, The Netherlands, 1986.

Kieffer, S.W., and C.H. Simonds, The role of volatiles and lithology in the impact cratering process, *Rev. Geophys. Space Phys.*, *18*, 143-181, 1980.

Kuz'min, R.O., N.N. Bobina, E.V. Zabalueva, and V.P. Shashkina, Structural inhomogeneities of the Martian cryolithosphere, *Solar Sys. Res.*, *22*, 121-133, 1988.

Lomov, I.N., M. Hiltl, O.Y. Vorobiev, and L.A. Glenn, Dynamic behavior of Berea sandstone for dry and water-saturated conditions, *Intl. J. Impact Engng.*, *26*, 465-474, 2001.

McGlaun, J.M., S.L. Thompson, and M.G. Elrick, CTH: A 3-dimensional shock-wave physics code, *Int. J. Impact Engng.*, *10*, 351-360, 1990.

Melosh, H.J., *Impact Cratering, A Geologic Process*, 245 pp., Oxford University Press, New York, 1989.

Melosh, H.J., and B.A. Ivanov, Impact crater collapse, *Annu. Rev. Earth Planet. Sci.*, *27*, 385-415, 1999.

Morgan, J., M. Warner, Chicxulub Working Group, J. Brittan, R. Buffler, A. Camargo, G. Christeson, P. Denton, A. Hildebrand, R. Hobbs, H. Macintyre, G. Mackenzie, P. Maguire, L. Marin, Y. Nakamura, M. Pilkington, V. Sharpton, D. Snyder, G. Suarez, and A. Trejo, Size and morphology and the Chicxulub impact crater, *Nature*, *390*, 472-476, 1997.

Mouginis-Mark, P.J., Morphology of Martian rampart craters, *Nature*, *272*, 691-694, 1978.

Mouginis-Mark, P.J., Martian fluidized crater morphology: Variations with crater size, latitude, altitude, and target material, *J. Geophys. Res.*, *84*, 8011-8022, 1979.

O'Keefe, J.D., and T.J. Ahrens, Planetary cratering mechanics, *J. Geophys. Res.*, *98*, 17011-17028, 1993.

O'Keefe, J.D., and T.J. Ahrens, Complex craters: Relationship of stratigraphy and rings to the impact conditions, *J. Geophys. Res.*, *104* (E11), 27091-27104, 1999.

O'Keefe, J.D., and T.J. Ahrens, Impact bulking, faulting and ejecta, *Lunar Planet. Sci. Conf., March 13-17, 2000 (abstract)*, *31*, 2000.

O'Keefe, J.D., and T.J. Ahrens, Hydrodynamic instabilities and planetary impact cratering, *Nature (submitted)*, 2002.

O'Keefe, J.D., S.T. Stewart, M.E. Lainhart, and T.J. Ahrens, Damage and rock-volatile mixture effects on impact crater formation, *Intl. J. Impact Engng.*, *26*, 543-553, 2001.

Pierazzo, E., and H.J. Melosh, Melt production in oblique impacts, *Icarus*, *145*, 252-261, 2000.

Scholz, C.H., The brittle plastic transition, in *Mechanics of Earthquakes and Faulting*, pp. 35-41, Cambridge Univ. Press, 1990.

Schultz, P.H., Atmospheric effects on ejecta emplacement, *J. Geophys. Res.*, *97*, 11623-11662, 1992.

Schultz, P.H., and D.E. Gault, Atmospheric effects on martian ejecta emplacement, *J. Geophys. Res.*, *84*, 7687-7699, 1979.

Squyres, S.W., S.M. Clifford, R.O. Kuzman, J.R. Zimbleman, and F.M. Costard, Ice in the Martian regolith, in *Mars*, edited by H.H. Kieffer, B.M. Jakosky, C.W. Snyder, and M.S. Mathews, pp. 523-556, U. Ariz. Press, Tucson, 1992.

Stewart, S.T., and T.J. Ahrens, Shock Hugoniot of water ice: abundant impact-induced melting in the solar system, *Geophys. Res. Lett. (submitted)*, 2002.

Swift, R.P., C.R. Hagelberg, T.C. Carney, and D. Greening, Modeling stress-induced damage from impact recovery experiments, in *ASME/ETCE Joint Conference on Energy for the New Millenium, Feb. 14-17, 2000*, New Orleans, LA, 2000.

Thompson, S.L., and H.S. Lauson, Improvements in the Chart D radiation-hydrodynamic Code III: Revised analytic equations of state, Sandia Laboratories, Albuquerque, NM, 1972, SC-RR-71 0714.